Multipole method for microstructured optical fibers. I. Formulation

T. P. White

School of Physics, University of Sydney, Sydney, New South Wales 2006, Australia

B. T. Kuhlmey

School of Physics, University of Sydney, Sydney, New South Wales 2006, Australia, and Institut Fresnel (Unité Mixte de Recherche du Centre National de la Recherche Scientifique 6133), Faculté des Sciences et Techniques de Saint Jérôme, 13397 Marseille Cedex 20, France

R. C. McPhedran

School of Physics, University of Sydney, Sydney, New South Wales 2006, Australia

D. Maystre and G. Renversez

Institut Fresnel (Unité Mixte de Recherche du Centre National de la Recherche Scientifique 6133), Faculté des Sciences et Techniques de Saint Jérôme, 13397 Marseille Cedex 20, France

C. Martijn de Sterke

School of Physics, University of Sydney, Sydney, New South Wales 2006, Australia

L. C. Botten

School of Mathematical Sciences, University of Technology, Sydney, New South Wales 2008, Australia

Received October 4, 2001; revised manuscript received May 7, 2002

We describe a multipole method for calculating the modes of microstructured optical fibers. The method uses a multipole expansion centered on each hole to enforce boundary conditions accurately and matches expansions with different origins by use of addition theorems. We also validate the method and give representative results. © 2002 Optical Society of America

OCIS codes: 060.2280, 060.2400, 060.4510.

1. INTRODUCTION

Microstructured optical fibers (MOFs)—fibers with multiple inclusions arranged about a core—have many remarkable properties such as large and adjustable dispersion and nonlinearity[1–4] and single-mode operation over a wide range of wavelengths.[5] They are also of theoretical interest because they incorporate a larger refractive index contrast than do conventional fibers and require a full electromagnetic treatment rather than the scalar or weak-guidance approximation.[6,7] Because the light confinement is due to many inclusions in a silica matrix rather than to a single doped region, the number of degrees of freedom, such as inclusion placement and diameter-to-spacing ratio, is larger than in conventional fibers.

To develop the potential of MOFs, accurate modeling tools are necessary. A range of methods has been developed, some of which use approximate scalar[5] or vector[8–10] treatments. A common strategy is to apply, in the transverse plane, periodic boundary conditions, enforced for example, by use of plane-wave expansions.[11,12] However, such supercell treatments effectively replace the necessarily finite MOF structure with an infinite one and thus cannot address the issue of the loss associated with propagation in a transversely finite confining structure. Plane-wave methods also do not accommodate general characteristics of the geometry of the inclusions. Whereas they are highly general, they are consequently not highly efficient.

One method that somewhat accommodates the shape of the expected modal field expands it in terms of Hermite–Gaussian functions.[3,13] However, these functions have intrinsic widths, which ideally match the width of the solution. Hence the method requires some *a priori* knowledge of the solution, which may not be available.

Beam propagation methods use a numerical algorithm to simulate the propagation of a coherent beam along a fiber,[14,15] from which the modes and their properties must be extracted *a posteriori*. Both scalar and vector versions of the algorithm are available, and fibers of any geometry

can be dealt with. One can calculate modal losses by observing the attenuation on propagation, but the propagation distance required increases as the loss decreases; this may be important in light of recent experiments[1] that demonstrated very low-loss (3.2-dB km^{-1}) MOFs.

Here we extend multipole formulations for multicore conventional fibers[16,17] to treat MOFs. A key aspect of the method described here is that it makes use of the circularity of the inclusions. It is therefore of high accuracy, converging sufficiently rapidly to be able to treat precisely systems that contain quite large numbers of inclusions. The formulation respects accurately the symmetry properties of modes in MOFs that have regularly arranged inclusions,[18,19] and indeed has been adapted to take into account those symmetry properties to increase computational efficiency. Furthermore, it yields both the real and the imaginary parts of the mode propagation constant; the latter gives the confinement loss associated with the finite extent of the MOF's set of confining inclusions. It can deal with the two types of MOF of current interest: those with a solid core, surrounded with air holes, and those with an air core (a cylindrical hole of somewhat larger radius), again surrounded by air holes, which tend to be more numerous than solid-core MOFs. Finally, the multipole method has frequency ω as an input parameter, with propagation constant β following from the calculation. It is thus well suited for calculations involving material dispersion. We stress that, though we consider only circular inclusions, the multipole method is not necessarily limited to these. Its extention to noncircular inclusions would follow along lines suggested by Felbacq *et al.*[20] We note that Yamashita *et al.* use a similar method for conventional multicore fibers.[21] However, they use a point-matching technique at the inclusion boundaries, whereas we enforce boundary conditions by projection of the field components onto an orthonormal basis.

Here we give the basic formulation of the method as well as some results. Kuhlmey *et al.* are preparing a companion paper,[22] in which they discuss the efficient implementation of the method as well as a number of results that are difficult to obtain by other methods and that thus demonstrate the unique features of the multipole method.

2. MULTIPOLE FORMULATION

Our formulation is similar to that of Lo *et al.*,[16] who considered the modes of high-index cylindrical inclusions in a low-index background. Therefore these structures have properly bound modes, irrespective of the geometry. In contrast, here the inclusions have a low index, and these therefore do not support bound modes. Rather, the modes arise from the geometry of the inclusions and, for a finite cladding, they are not bound but leaky. This difference has important consequences for the method, and we therefore describe it in some detail here. We concentrate on solid-core MOFs, with the modifications for air-core MOFs discussed in passing.

The geometry that we treat is given in Fig. 1; it represents a transverse xy cut of the fiber, which is infinitely extended along the z axis. It shows a silica matrix of (real) refractive index n_e, perforated with a finite number

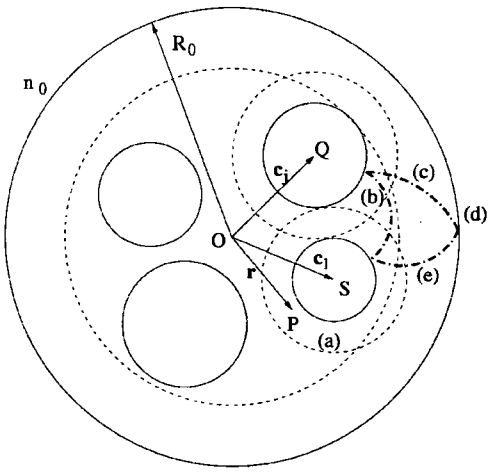

Fig. 1. Geometry of the MOFs considered, together with the contributions to the fields just outside a generic hole i. Regions of convergence of multipole expansions are indicated by dashed curves. Note that QP is $\mathbf{r}_j$ in Eq. (8), and SP is $\mathbf{r}_l$ and OP is $\mathbf{r}$. Solid curves indicate physical boundaries; dashed curves indicate regions of convergence.

N_c of inclusions indexed by i and of diameter d_i, whose centers are specified by $\mathbf{c}_i$. The refractive index of the inclusions is n_i. In the numerical examples $n_i = 1$, and all inclusions have the same diameter d, except for air-guided MOFs for which the central hole is larger than the others. The air holes are always hexagonally packed and regularly spaced with separation Λ.

Outside this hole region the MOF is enclosed in a jacket (radius $r > R_0$), whose index n_0 may be complex. One choice for this is to take a jacket with refractive index 1, simulating a MOF in air or vacuum. Doing so would enable us to investigate modes confined between the microstructured part of the fiber and the air region as well as effects that are due to the finite nature of the silica region surrounding fibers. More generally, our method can deal with any type of cladding surrounding the structure.

A. Choice of Propagating Fields

We characterize in the complex representation the electric and magnetic fields $\mathcal{E}$ and $\mathcal{H}$ in the MOF by specifying the components $\mathcal{E}_z$ and $\mathcal{H}_z$ along the fiber axis, with transverse fields following from Maxwell's equations.[6] In fact, it is convenient to work with scaled magnetic fields: $\mathcal{K} = Z\mathcal{H}$, where Z denotes the impedance of free space. Each mode is characterized by its propagation constant β and by the transverse dependence of the fields:

$$\mathcal{E}(r, \theta, z, t) = \mathbf{E}(r, \theta)\exp[i(\beta z - \omega t)], \quad (1)$$

$$\mathcal{K}(r, \theta, z, t) = \mathbf{K}(r, \theta)\exp[i(\beta z - \omega t)], \quad (2)$$

where ω denotes the angular frequency, which is related to the free-space wave number by $\omega = kc$. Note that β is complex for leaky modes; the imaginary part of β accounts for attenuation along the z axis. Here we use the modes' effective index, which is related to β by $n_{\text{eff}} = \beta/k$.

Each of the fields ($V = E_z$ or $V = K_z$) satisfies the Helmholtz equation

$$[\nabla^2 + (k_\perp^e)^2]V = 0 \quad (3)$$

in the matrix, where $k_\perp^e = (k^2 n_e^2 - \beta^2)^{1/2}$, and

$$[\nabla^2 + (k_\perp^i)^2]V = 0 \tag{4}$$

in the holes, where $k_\perp^i = (k^2 n_i^2 - \beta^2)^{1/2}$. Care is required when one is computing complex square roots: For forward-propagating modes that attenuate as they propagate in the $+z$ direction, we require that $\Re(\beta) > 0$ and $\Im(\beta) > 0$. Assuming for now that $n_0^2 k^2$ is real, and because $k_\perp^J = (k^2 n_0^2 - \beta^2)^{1/2}$, then $\Re(\beta)\Im(\beta) + \Re(k_\perp^J) \times \Im(k_\perp^J) = 0$, so $\Re(k_\perp^J)\Im(k_\perp^J) < 0$. Thus $k_\perp^J$ lies in either the second or the fourth quadrant of the complex plane. In fact, we must choose the fourth quadrant[6,7] to ensure that the outgoing waves have the correct behavior of taking energy away from the fiber. We treat the case in which n_0 has a small imaginary part by continuity.

B. Formulation of the Field Identities

In the vicinity of the lth cylindrical inclusion (see Fig. 1) we represent the fields in the matrix in local coordinates $\mathbf{r}_l = (r_l, \theta_l) = \mathbf{r} - \mathbf{c}_l$ and express the fields in Fourier–Bessel series, a natural basis for harmonic functions in cylindrical coordinates. $J_m(z)$ and $H_m^{(1)}(z)$ are the usual Bessel function of order m and the Hankel function of the first kind of order m, respectively; thus we have for the electric field

$$Ez = \sum_m [A_m^{El} J_m(k_\perp^e r_l) + B_m^{El} H_m^{(1)}(k_\perp^e r_l)]\exp(im\theta_l), \tag{5}$$

and similarly for K_z, but with coefficients A_m^{Kl} and B_m^{Kl}. In Eq. (5) the J_m terms represent the regular incident part $\mathcal{R}^{El}$ of field E_z for cylinder l because it is finite everywhere, whereas the $H_m^{(1)}$ terms represent the outgoing wave part $\mathcal{O}^{El}$ of the field, which is associated with a source at the center of the cylinder. We thus have $E_z = \mathcal{R}^{El} + \mathcal{O}^{El}$.

Local expansion (5) is valid only in an annulus extending from the surface of the cylinder to the nearest cylinder or source [region (a) in Fig. 1]. The same expression may be used around the jacket boundary, which we designate with a superscript 0 [region (d) in Fig. 1].

Another description of the fields is orginally due to Wijngaard.[23] He reasoned that a field in a region can be written as a superposition of outgoing waves from all source bodies in the region. If the waves originate outside the region, their expansion is expressed in terms of J-type waves, which are source free. Of course this physical argument can be supplemented by rigorous mathematical arguments,[16,23,24] as discussed in Appendix A. For MOFs the Wijngaard expansion takes the form

$$E_z = \sum_{l=1}^{N_c} \sum_m B_m^{El} H_m^{(1)}(k_\perp^e |\mathbf{r}_l|)\exp[im\ \arg(\mathbf{r} - \mathbf{c}_l)] + \sum_m A_m^{E0} J_m(k_\perp^e r)\exp(im\theta). \tag{6}$$

Each term of the m series is an outgoing wave field with a source at cylinder l, whereas the final term, indexed by 0, is the regular field originating at the jacket boundary.

Equating Eqs. (5) and (6), thus enforcing consistency, yields, in the vicinity of cylinder l,

$$\sum_m A_m^{El} J_m(k_\perp^e r_l)\exp(im\theta_l) = \sum_{\substack{j=1 \\ j\neq l}}^{N} \sum_m B_m^{Ej} H_m^{(1)}(k_\perp^e r_j)\exp(im\theta_j) + \sum_m A_m^{E0} J_m(k_\perp^e r)\exp(im\theta), \tag{7}$$

because the $H_m^{(1)}(k_\perp^e r_l)$ terms are common to both expansions. Evaluating this expression is not straightforward because different terms refer to different origins. We therefore use Graf's addition theorem,[25] which lets us transform the origin of the cylindrical waves. A full discussion is given in Appendix B, where we show that it may be viewed as a change of basis transformation. For example, the contribution to the local regular field in the vicinity of cylinder l that is due to cylinder j [curve (b), Fig. 1] is

$$\sum_n A_n^{Elj} J_n(k_\perp^e r_l)\exp[in\ \arg(\mathbf{r}_l)] = \sum_m B_m^{Ej} H_m^{(1)}(k_\perp^e r_j)\exp[im\ \arg(\mathbf{r}_j)], \tag{8}$$

where

$$A_n^{Elj} = \sum_m \mathcal{H}_{nm}^{lj} B_m^{Ej}, \tag{9}$$

$$\mathcal{H}_{nm}^{lj} = H_{n-m}^{(1)}(k_\perp^e c_{lj})\exp[-i(n-m)\arg(\mathbf{c}_{lj})], \tag{10}$$

where $\mathbf{c}_{lj} = \mathbf{c}_j - \mathbf{c}_l$, as shown in Appendix B.1. At this point we introduce the notation $\mathbf{A}^{Elj} = [A_n^{Elj}]$, which lets us generate vectors of mathematical objects. Similar notation is used for matrices, i.e., $\boldsymbol{\mathcal{H}}^{lj} = [\mathcal{H}_{nm}^{lj}]$. In matrix form, then, we represent basis change (9) as

$$\mathbf{A}^{Elj} = \boldsymbol{\mathcal{H}}^{lj}\mathbf{B}^{Ej}. \tag{11}$$

Similarly, the contribution to the regular incident field at cylinder l that is due to the jacket [curve (e), Fig. 1] is

$$\sum_n A_n^{El0} J_n(k_\perp^e r_l)\exp[in\ \arg(\mathbf{r}_l)] = \sum_m A_m^{E0} J_m(k_\perp^e r)\exp(im\theta), \tag{12}$$

where the change of basis (derived in Appendix B.2) is

$$\mathbf{A}^{El0} = \boldsymbol{\mathcal{J}}^{l0}\mathbf{A}^{E0}, \tag{13}$$

with

$$\boldsymbol{\mathcal{J}}^{l0} = [\mathcal{J}_{nm}^{l0}] = \{(-1)^{(n-m)} J_{n-m}(k_\perp^e c_l) \times \exp[i(m-n)\arg(\mathbf{c}_l)]\}. \tag{14}$$

Accumulating these contributions for all cylinders and the jacket, we have, in annulus (a) about cylinder l (see Fig. 1)

$$\mathbf{A}^{El} = \sum_{\substack{j=1 \\ j\neq l}}^{N_c} \mathbf{A}^{Elj} + \mathbf{A}^{El0} = \sum_{\substack{j=1 \\ j\neq l}}^{N_c} \mathcal{H}^{lj}\mathbf{B}^{Ej} + \mathcal{J}^{l0}\mathbf{A}^{E0}, \tag{15}$$

a result that holds for both the E_z and the K_z fields.

In a similar way, the outgoing field in the vicinity of the jacket boundary that is due to cylinder j [curve (c)] is

$$\sum_n B_n^{E0j} H_n^{(1)}(k_\perp^e r)\exp(in\theta) = \sum_m B_m^{Ej} H_m^{(1)}(k_\perp^e r_j)\exp[im\arg(\mathbf{r}_j)], \tag{16}$$

with the change of basis represented by

$$\mathbf{B}^{E0j} = \mathcal{J}^{0j}\mathbf{B}^{Ej}, \tag{17}$$

where

$$\mathcal{J}^{0j} = [\mathcal{J}_{nm}^{0j}] = \{J_{n-m}(k_\perp^e c_j)\exp[-i(n-m)\arg(\mathbf{c}_j)]\}, \tag{18}$$

as shown in Appendix B.3.

Adding the contributions for all cylinder sources, we re-express the first term on the right-hand side of Wijngaard expansion (6) in a form that is valid just inside the jacket [region (d)]:

$$\sum_{l=1}^{N_c} \mathcal{O}^{El} = \sum_n B_n^{E0} H_n^{(1)}(k_\perp^e r)\exp(in\theta) = \mathcal{O}^{E0}, \tag{19}$$

where

$$\mathbf{B}^{E0} = \sum_{l=1}^{N_c} \mathbf{B}^{E0l} = \sum_{l=1}^{N_c} \mathcal{J}^{0l}\mathbf{B}^{El}, \tag{20}$$

a result that also holds for both E_z and K_z.

C. Boundary Conditions and Field Coupling

Whereas the field identities of Subsection 2.A apply individually to each field component, cross coupling between them occurs at boundaries. In what follows, it is most convenient to formulate the boundary conditions in terms of cylindrical reflection coefficients as derived in Appendix C. For circular inclusions, for the reflected fields outside each cylinder we have

$$\begin{aligned} B_n^{El} &= R_n^{EEl}A_n^{El} + R_n^{EKl}A_n^{Kl}, \\ B_n^{Kl} &= R_n^{KEl}A_n^{El} + R_n^{KKl}A_n^{Kl}, \end{aligned} \tag{21}$$

where the expression for the reflection coefficients are given in Eqs. (C11) of Appendix C. The reflection matrices are derived for each inclusion treated in isolation and are thus known in closed form for circular inclusions, in which case they are diagonal. For noncircular inclusions they could be replaced by either analytic expressions for other special cases or numerical estimates from a differential or integral equation treatment.[20,26] In these cases they generally also have off-diagonal elements.

Equations (21) can be written as

$$\begin{bmatrix} \mathbf{B}^{El} \\ \mathbf{B}^{Kl} \end{bmatrix} = \begin{bmatrix} \mathbf{R}^{EEl} & \mathbf{R}^{EKl} \\ \mathbf{R}^{KEl} & \mathbf{R}^{KKl} \end{bmatrix} \begin{bmatrix} \mathbf{A}^{El} \\ \mathbf{A}^{Kl} \end{bmatrix}, \tag{22}$$

or

$$\tilde{\mathbf{B}}^l = \tilde{\mathbf{R}}^l\tilde{\mathbf{A}}^l, \tag{23}$$

with $\mathbf{R}^{EE,l} = \mathrm{diag}(R_n^{EEl})$ and similar definitions for the other reflection matrices. We also need an interior form at the jacket boundary [point (d) in Fig. 1]:

$$\tilde{\mathbf{A}}^0 = \tilde{\mathbf{R}}^0\tilde{\mathbf{B}}^0, \tag{24}$$

where $\tilde{\mathbf{A}}^0$, $\tilde{\mathbf{B}}^0$, and $\tilde{\mathbf{R}}^0$ are defined as in Eqs. (22) and (23) and the coefficients of $\tilde{\mathbf{R}}^0$ are given by Eqs. (C7). In this form the outgoing field ($\tilde{\mathbf{B}}^0$) generated by all inclusions [curve (c)] is reflected by the jacket to generate the regular field ($\tilde{\mathbf{A}}^0$), which feeds into the incident field for inclusion l [curve (e) in Fig. 1]. It is straightforward to adapt $\tilde{\mathbf{R}}^0$ to cases in which multiple films surround the hole region.

D. Derivation of the Rayleigh Identity

With the structure of the field coupling derived in Subsection 2.C we now form field identities that apply to the vector components $\tilde{\mathbf{A}}^l$ and $\tilde{\mathbf{B}}^l$. From Eq. (15) we have

$$\tilde{\mathbf{A}}^l = \sum_{\substack{j=1 \\ j\neq l}}^{N_c} \tilde{\mathcal{H}}^{lj}\tilde{\mathbf{B}}^j + \tilde{\mathcal{J}}^{l0}\tilde{\mathbf{A}}^0, \tag{25}$$

where $\tilde{\mathcal{H}}^{lj} = \mathrm{diag}(\mathcal{H}^{lj}, \mathcal{H}^{lj})$ and $\tilde{\mathcal{J}}^{l0} = \mathrm{diag}(\mathcal{J}^{l0}, \mathcal{J}^{l0})$. Equation (25) is the representation of the regular incident field at cylinder l in terms of outgoing components $\tilde{\mathbf{B}}^j$ from all other cylinders and an incident field contribution $\tilde{\mathbf{A}}^0$ from the jacket.

Combining Eq. (25) for all cylinders $l = 1 \ldots N_c$ and introducing $\mathcal{A} = [\tilde{\mathbf{A}}^l]$ and $\mathcal{B} = [\tilde{B}^l]$, we derive

$$\mathcal{A} = \tilde{\mathcal{H}}\mathcal{B} + \tilde{\mathcal{J}}^{B0}\tilde{\mathbf{A}}^0, \tag{26}$$

where $\tilde{\mathcal{H}} = [\tilde{\mathcal{H}}^{lj}]$ for $l, j = 1 \ldots N_c$ with $\tilde{\mathcal{H}}^{ll} \equiv \mathbf{0}$ and

$$\tilde{\mathcal{J}}^{B0} = [(\tilde{\mathcal{J}}^{l0}] = [(\tilde{\mathcal{J}}^{10})^T, (\tilde{\mathcal{J}}^{20})^T, \ldots, (\tilde{\mathcal{J}}^{N_c0})^T]^T, \tag{27}$$

where T indicates the transpose. Similarly, the vector outgoing field in the vicinity of the jacket that is due to all the cylinders is given by

$$\tilde{\mathbf{B}}^0 = \sum_{j=1}^{N_c} \tilde{\mathcal{J}}^{0l}\tilde{\mathbf{B}}^l = \tilde{\mathcal{J}}^{0B}\tilde{\mathcal{B}} \tag{28}$$

from Eq. (20). Here

$$\tilde{\mathcal{J}}^{0B} = [\tilde{\mathcal{J}}^{0l}] = [\tilde{\mathcal{J}}^{01}, \tilde{\mathcal{J}}^{02}, \ldots \tilde{\mathcal{J}}^{0N_c}]. \tag{29}$$

Combining Eqs. (23), (24), (26), and (28) and eliminating $\tilde{\mathbf{A}}^0$ and $\tilde{\mathbf{B}}^0$, we form a homogeneous system of equations (Rayleigh identity) in the source coefficients:

$$[\mathbf{I} - \mathcal{R}(\tilde{\mathcal{H}} + \tilde{\mathcal{J}}^{B0}\tilde{\mathbf{R}}^0\tilde{\mathcal{J}}^{0B})]\mathcal{B} \equiv \mathcal{M}\mathcal{B} = \mathbf{0}, \tag{30}$$

where the right-hand side indicates the absence of external sources and

$$\mathcal{R} = \mathrm{diag}[\tilde{\mathbf{R}}^1, \tilde{\mathbf{R}}^2, \ldots, \tilde{\mathbf{R}}^{N_c}]. \tag{31}$$

Nontrivial solutions to homogeneous system (30) correspond to nonzero fields propagating in the z direction.

The solutions represent a nonzero field that exists without any exterior source of energy, in other words, propagating (possibly leaky) fiber modes.

3. NUMERICAL CONSIDERATIONS

A. Mode Location

Homogeneous equation (30), the main result of this paper, corresponds to a nontrivial field vector $\mathcal{B}$ only if the determinant of matrix $\mathcal{M}$ is effectively zero. Once the structure and the wavelength are given, matrix $\mathcal{M}$ depends only on β, or, equivalently, on its effective index n_{eff}. The search for modes therefore becomes a matter of finding zeros of the complex function $\det(\mathcal{M})$ of the complex variable n_{eff}. To find the modes numerically, one must truncate field expansions such as Eq. (5), say, to have m running from $-M$ to M. In Fig. 2 we show a determinant surface in the neighborhood of a well-defined minimum, corresponding to a mode with a well-characterized propagation constant $n_{\text{eff}} = 1.43858501 + 4.986 \times 10^{-7} i$. This example, and those that follow, refer to a structure with a single ring of six equally spaced holes with $d = 5\ \mu\text{m}$, $\Lambda = 6.75\ \mu\text{m}$, $\lambda = 1.45\ \mu\text{m}$, $R_0 = 14.25\ \mu\text{m}$, $n_e = 1.45$, $n_0 = n_e + 10^{-8} i$, and $M = 5$. The small imaginary part of n_0 has been introduced for mathematical convenience. Its existence is not essential in computations, and its exact value does not have a significant effect on results.

We know from a group theoretical study of waveguides by McIsaac[18] that the modes of the fibers that we are considering are either nondegenerate or doubly degenerate. Inasmuch as $\det(\mathcal{M})$ is the product of the eigenvalues of $\mathcal{M}$, we must look for minima in which one or two of the eigenvalues have magnitudes that are substantially smaller than the others. However, a minimum of the determinant may also correspond to more than two eigenvalues being small simultaneously (a false minimum). To distinguish these from genuine solutions, we consider the singular values[27] of **M**, which, for our case, correspond to the magnitudes of the eigenvalues. False minima can be distinguished by a singular value decomposition at the putative minimum. Assuming that we have a genuine minimum, the accuracy of the singular values may be assessed from the stability of n_{eff} with increasing truncation

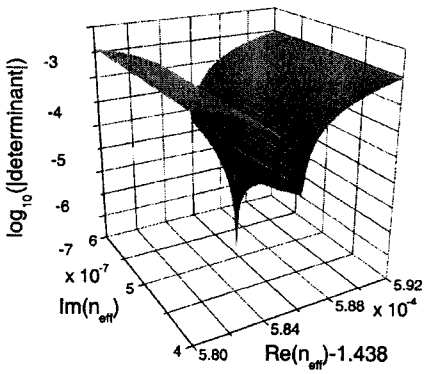

Fig. 2. Logarithm of the magnitude of the determinant of $\mathcal{M}$ versus the real and the imaginary parts of the complex refractive index for the MOF given in the text.

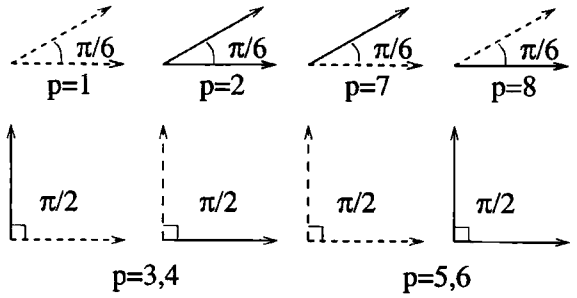

Fig. 3. Minimum sectors for waveguides with C_{6v} symmetry. Mode classes $p = 1, 2, 7, 8$ are nondegenerate; $p = 3, 4$ and $p = 5, 6$ are twofold degenerate. Solid lines indicate Dirichlet boundary conditions for the electric field; dashed lines indicate Neumann boundary conditions.

order. In most cases the real part of n_{eff} is found to ten decimal places, and the imaginary part to five significant figures, whereas the ratio of the smallest singular values and the next smallest is approximately 7 orders of magnitude. Another useful diagnostic of false minima is that they often have real n_{eff}, whereas genuine roots have a nonzero imaginary part. These distinguishing criteria are further discussed in Ref. 22.

The null vectors that correspond to small singular values are approximate solutions to field identity (30). For nondegenerate modes the null vector is unique to within an arbitrary multiplicative constant. For a twofold degenerate mode we let the basis states be prescribed by group theory (see Subsection 3.B), though any linear combination of these is equally justified.

B. Symmetry Properties of Modes

McIsaac[18] classified the electromagnetic modes of waveguide structures according to the symmetry properties of the configuration. This approach was previously exploited by Yamashita *et al.*[21] for modal analysis of conventional multicore fibers. The point group most often encountered in MOF studies is C_{6v} because it combines sixfold symmetry with mirror symmetry. Assuming C_{6v} symmetry leads immediately to a number of conclusions: Any mode belongs to one of eight classes, and the classes are either nondegenerate (classes 1, 2, 7, 8), in which case they exhibit the full symmetry of the structure, or twofold degenerate (classes 3–6), in which case they exhibit the full symmetry in an appropriate linear combination. Inasmuch as the nondegenerate modes have the full symmetry of the structure, their field needs to be calculated only in a minimum sector of 30°, the edges of which must coincide with a symmetry axis of the structure, with the field elsewhere following by symmetry. The difference between the modal classes are that different boundary conditions apply to the tangential component of the electric field at the edges of the minimum sector; these are either Neumann ($\partial E_z / \partial \theta = 0$) or Dirichlet ($E_z = 0$) conditions or combinations of these (see Fig. 3). For the degenerate mode classes the minimum sector is 90° (Fig. 3).

Table 1 lists the first ten modes for the MOF that we are considering, exemplifying all McIsaac's[18] eight mode classes. The losses (in decibels per meter) listed in column 3 are obtained from the imaginary part of n_{eff} by

$$\mathcal{L} = \frac{20}{\ln(10)} \frac{2\pi}{\lambda} \Im(n_{\text{eff}}) \times 10^6, \tag{32}$$

with λ in micrometers. In Table 1 the losses are large because more than one ring is necessary to achieve losses compatible with practical usage, as we discuss further in Ref. 22.

We show the fields of the first three modes from Table 1 in Figs. 4–6. Figure 4 shows a mode with a vertical nodal line for E_z and a horizontal antinodal line. It must therefore belong to class $p = 3$ in Fig. 3, one of a degenerate pair. Its companion ($p = 4$) is shown in Fig. 5. The similarity between $|E_z|$ in Fig. 4 and $|K_z|$ in Fig. 5 is often evident in degenerate MOF modes but is not exact,

Table 1. Effective Index, Loss, Mode Class, and Degeneracy of the First 10 Modes of the MOF Given in the Text, Calculated for $M=5$

n_{eff}		Loss	Class	Degeneracy
Real	Imaginary	(dB/m)	(p)	
1.445395345	3.15×10^{-8}	1.2	3,4	2
1.438585801	4.986×10^{-7}	20	2	1
1.438445842	9.929×10^{-7}	37	5,6	2
1.438366726	1.374×10^{-6}	52	1	1
1.430175	2.22×10^{-5}	840	8	1
1.4299694	1.577×10^{-5}	590	3,4	2
1.429255296	9.337×10^{-6}	350	7	1

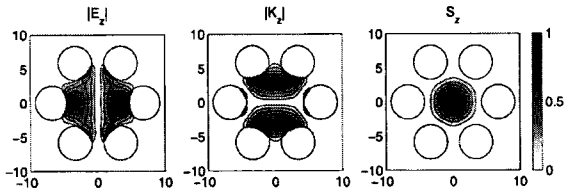

Fig. 4. Normalized fields $|E_z|$ and $|K_z|$ and energy flow S_z for the degenerate fundamental mode class $p = 3$ for a six-hole MOF, with data of Fig. 2 and $n_{\text{eff}} = 1.445395345 + 3.15 \times 10^{-8} i$.

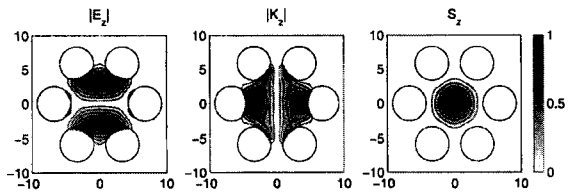

Fig. 5. Similar to Fig. 4 but for degenerate fundamental mode class with $p = 4$ and $n_{\text{eff}} = 1.445395345 + 3.15 \times 10^{-8} i$.

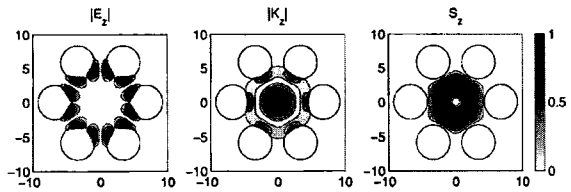

Fig. 6. Similar to Fig. 4 but for nondegenerate mode with $p = 2$ and $n_{\text{eff}} = 1.438585801 + 4.986 \times 10^{-7} i$.

because E_z and K_z satisfy different boundary conditions. The nondegenerate mode (Fig. 6) displays the MOF's full sixfold symmetry and has nodes of E_z at angles 0° and 30°; it thus belongs to class $p = 2$ (Fig. 3).

4. DISCUSSION AND CONCLUSIONS

We have given the basic formulation of our multipole method, and we have shown that it allows one to calculate the modal properties of MOFs. The results presented show the level of detail that can be obtained in calculating field structures and symmetry properties. It is at present limited to designs composed of nonintersecting circular inclusions, but nevertheless it can be employed in studies ranging over a wide parameter space: hole radius, spacing, number of rings, packing geometry, air or solid core, etc. A key feature of the method is that frequency ω can be used as an input parameter, whereas the propagation constant β follows from the calculation. This is an important advantage when one is dealing with dispersive media: Because ω is fixed, the appropriate refractive indices are known from the outset. Contrast this with plane-wave methods, for example, in which β is fixed and ω follows from the calculation. The appropriate refractive indices are then not known and are usually included by use of an iterative procedure, adding considerably to the computational requirements.

The magnitude of matrix $\mathcal{M}$ in identity (30) equals $2(2M + 1)N_c$ and is thus moderate if the number of holes is not too large. In addition, as discussed in Ref. 22, M needs to increase with the size of the holes. We also detail there the method's implementation and validation and also give more numerical results. Therefore we defer further discussions of the method to Ref. 22.

APPENDIX A: DERIVATION OF THE WIJNGAARD EXPANSION

To generalize the Wijngaard expansion of the field to MOF, we define a function $U(x, y)$ as

$$U(x, y) = \begin{cases} E_z & r < R_0 \\ 0 & \text{elsewhere} \end{cases}. \tag{A1}$$

Thus U is continuous inside the hole region because of the continuity of the tangential field component, whereas its normal derivative is discontinuous at the boundaries of the inclusions. Both U and its normal derivative are discontinuous at jacket boundary C ($r = R_0$). As a consequence, it can be deduced from Eqs. (3) and (4) that U satisfies, in the sense of distributions,[28]

$$\nabla^2 U + k_\perp^2 U = s, \tag{A2}$$

where $k_\perp = k_\perp^i$ in inclusion i and where $k_\perp = k_\perp^e$ elsewhere. Source s is a singular distribution, given by

$$s = \sum_{j=1}^{N_c} S_j \delta_{C_j} - T \delta_C - \nabla \cdot (\mathbf{n} Q \delta_C), \tag{A3}$$

with S_j defined at boundary C_j of the jth hole as the jump of the normal derivative of U. Further, Q and T are, respectively, the limits of U and its normal derivative at r

$= R_0$, where the normal $\mathbf{n}$ is outwardly oriented. Distribution $A\,\delta_C$ is defined by[28]

$$\langle A\,\delta_C\,,\,\varphi\rangle = \int_C A(M)\varphi(M)\mathrm{d}M, \tag{A4}$$

where M is a point of C, $\mathrm{d}M$ is the length of an elementary segment of C, and φ is an infinitely differentiable function with bounded support.

Equation (A2) can be rewritten as

$$\nabla^2 U + (k_\perp^e)^2 U = [(k_\perp^e)^2 - (k_\perp)^2]U + s, \tag{A5}$$

so in the hole region U follows from the convolution

$$U = G_e \star \{s + [(k_\perp^e)^2 - (k_\perp)^2]U\}, \tag{A6}$$

where G_e is the Green function of the Helmholtz equation: $G_e = -iH_0^{(1)}(k_\perp^e r)/4$. From Eqs. (A3) and (A6), U can be reexpressed as

$$U = \sum_{j=1}^{N_c} G_e \star D_j + G_e \star D, \tag{A7}$$

with

$$D_j = S_j \delta_{C_j} + [(k_\perp^e)^2 - (k_\perp^j)^2]U_j\,, \tag{A8}$$

$$D = -T\delta_C - \nabla \cdot (\mathbf{n}Q\,\delta_C), \tag{A9}$$

$$U_j = \begin{cases} U & \text{in the } j\text{th inclusion} \\ 0 & \text{elsewhere} \end{cases}. \tag{A10}$$

Each term $V_j = G_e \star D_j$ of the sum on the right-hand side of Eq. (A7) is generated by sources placed inside or at the boundary of the jth inclusion and satisfies a radiation condition outside this hole. It can be identified at any point outside this inclusion as the field scattered by this conclusion. Of course, because it satisfies the homogeneous Helmholtz equation outside the jth inclusion, in the sense of distributions it can be represented in the entire matrix region as a Fourier–Bessel series:

$$V_j = \sum_m B_m^{Ej} H_m^{(1)}(k_\perp^e r_j)\exp(im\,\theta_j). \tag{A11}$$

The term $G_e \star D$ on the right-hand side of Eq. (A7) is generated by sources on the jacket boundary, and it thus has no singularity inside this boundary. It can be identified as the incident field generated by the jacket and illuminating the matrix-inclusion region. It can also be represented in a Fourier–Bessel expansion:

$$V_{\mathrm{inc}} = \sum_m A_m^{E0} J_m(k_\perp^e r)\exp(im\,\theta). \tag{A12}$$

From Eqs. (A7), (A11), and (A12) it can now be shown that, in the entire matrix region, field E_z can be represented by Wijngaard expansion (6). The same argument can be used for the z component of magnetic field H_z.

APPENDIX B: CHANGE OF BASIS

Three changes of basis transformation are required: (i) conversion of outgoing fields sourced on one cylinder to regular fields in the basis of another cylinder, (ii) conversion of the regular field sourced on the jacket boundary to a regular field in the basis of each cylinder, and (iii) conversion of outgoing fields sourced at the cylinders to an outgoing field close to the jacket boundary. These are considered separately below.

1. Cylinder-to-Cylinder Conversion

Here we consider an outgoing cylindrical harmonic wave sourced from cylinder j and derive its regular representation in the coordinate system of cylinder l. From Graf's theorem[25] we derive

$$H_m^{(1)}(k_\perp^e r_j)\exp[im\,\arg(\mathbf{r}_j)] = \sum_{n=-\infty}^{\infty} J_n(k_\perp r_l)\exp[in\,\arg(\mathbf{r}_l)]H_{n-m}^{(1)}(k_\perp^e c_{lj}) \times \exp[-i(n-m)\arg(\mathbf{c}_{lj})], \tag{B1}$$

so the total field that is due to cylinder j is expressed as

$$\sum_{m=-\infty}^{\infty} B_m^j H_m^{(1)}(k_\perp^e r_j)\exp[im\,\arg(\mathbf{r}_j)] = \sum_{n=-\infty}^{\infty} A_n^{lj} J_n(k_\perp^e r_l)\exp[in\,\arg(\mathbf{r}_l)], \tag{B2}$$

where A_n^{lj}, defined in Eqs. (9) and (10), denotes the contribution to the nth multipole coefficient at cylinder l that is due to cylinder j.

2. Jacket-to-Cylinder Conversion

From Graf's theorem[25] we now have

$$J_m(k_\perp^e r)\exp(im\,\theta) = \sum_{n=-\infty}^{\infty} J_n(k_\perp^e r_l)\exp[in\,\arg(\mathbf{r}_l)] \times (-1)^{n-m} J_{n-m}(k_\perp^e c_l) \times \exp[-i(n-m)\arg(\mathbf{c}_l)], \tag{B3}$$

and, from this, the change in the basis transform is

$$\sum_{m=-\infty}^{\infty} A_m^0 J_m(k_\perp^e r)\exp(im\,\theta) = \sum_{n=-\infty}^{\infty} A^{l0} J_n(k_\perp^e r_l)\exp[in\,\arg(\mathbf{r}_l)], \tag{B4}$$

where A_n^{l0} denotes the multipole coefficient in the basis of cylinder l that is due to the regular field radiating from the jacket. Equation (13) is the matrix form of Eq. (B4).

3. Cylinder-to-Jacket Conversion

The relevant transformation from Graf's theorem[25] is now

$$H_m^{(1)}(k_\perp^e r_l)\exp[im\,\arg(\mathbf{r}_l)] = \sum_{n=-\infty}^{\infty} H_n^{(1)}(k_\perp^e r)\exp(in\,\theta)J_{n-m}(k_\perp^e c_l) \times \exp[-i(n-m)\arg(\mathbf{c}_l)]. \tag{B5}$$

The contribution from cylinder l to the outgoing field near the jacket boundary is

$$\sum_{m=-\infty}^{\infty} B_m^l H_m^{(1)}(k_\perp^e r_l)\exp[im\arg(\mathbf{r}_l)]$$

$$= \sum_{n=-\infty}^{\infty} B_n^{0l} H_n^{(1)}(k_\perp^e r)\exp(in\theta), \quad \text{(B6)}$$

which can be written in matrix notation as Eq. (17).

APPENDIX C: BOUNDARY CONDITIONS—REFLECTION MATRICES

We consider a cylinder centered at the origin of refractive index n_- and radius a embedded in a medium of refractive index n_+. To derive the reflection matrices of this cylinder we express the E_z and H_z fields in terms of Fourier–Bessel series in the local cylindrical coordinates (r, θ) inside and outside the cylinder [cf. Eq. (5)]:

$$E_z^{\mp}(r, \theta) = \sum_{m=-\infty}^{\infty} [A_m^{E\mp} J_m(k_\perp^{\mp} r) + B_m^{E\mp} H_m^{(1)} \times (k_\perp^{\mp} r)]\exp(im\theta) \quad \text{(C1)}$$

for $r < a$ $(-)$ and $r > a$ $(+)$, with similar expressions for K_z. Here $k_\perp^{\pm} = (k^0{}^2 n_{\pm}^2 - \beta^2)^{1/2}$ are the transverse wave numbers inside (outside) the cylinder. We introduce the vectors $\mathbf{A}^{E\pm} = [A_m^{E\pm}]$ and $\mathbf{B}^{E\pm} = [B_m^{E\pm}]$, as well as their K counterparts, and the condensed notation introduced in Eqs. (22) and (23) for $\tilde{\mathbf{A}}^{\pm}$ and $\tilde{\mathbf{B}}^{\pm}$. The interpretation of the J and H terms was made in Section 2. At the cylinder boundary, reflection and transmission occur and the waves mix with one another, which, because of the linearity of the Maxwell equations, can be expressed as a matrix relation among the various coefficients, as

$$\tilde{\mathbf{A}}^- = \tilde{\mathbf{T}}^- \tilde{\mathbf{A}}^+ + \tilde{\mathbf{R}}^- \tilde{\mathbf{B}}^-,$$

$$\tilde{\mathbf{B}}^+ = \tilde{\mathbf{R}}^+ \tilde{\mathbf{A}}^+ + \tilde{\mathbf{T}}^+ \tilde{\mathbf{B}}^-. \quad \text{(C2)}$$

Here $\mathbf{R}^-$ and $\mathbf{R}^+$ are referred to as interior and exterior reflection matrices of the cylinder, whereas $\mathbf{T}^+$ and $\mathbf{T}^-$ are transmission matrices, which do not matter in the analysis below. Note that the first of Eqs. (C2) leads to Eq. (24), whereas the second leads to Eq. (23).

The $\mathbf{R}^{\pm}$ matrices can be derived from the continuity of the tangential field components at the cylinder boundary. To make this derivation we need the expressions for the θ components of the fields, which can be expressed as functions of the z components as[6]

$$E_\theta(r, \theta) = \frac{i}{k_\perp^2}\left(\frac{\beta}{r}\frac{\partial E_z}{\partial \theta} - k\frac{\partial K_z}{\partial r}\right), \quad \text{(C3)}$$

$$K_\theta(r, \theta) = \frac{i}{k_\perp^2}\left(\frac{\beta}{r}\frac{\partial K_z}{\partial \theta} + kn^2\frac{\partial E_z}{\partial r}\right), \quad \text{(C4)}$$

where n is the refractive index. The partial derivatives that appear follow straightforwardly from Eq. (C1).

We can now write the continuity conditions for the z components by equating Eq. (C1) on the boundary. Because the resultant equation is valid for all θ, terms with different m decouple, and we find for each m that

$$A_m^{E-} J_m^- + B_m^{E-} H_m^- = A_m^{E+} J_m^+ + B_m^{E+} H_m^+, \quad \text{(C5)}$$

with the same result for K_z. Here we have introduced the condensed notation $J_m^{\pm} = J_m(k_\perp^{\pm} a)$, etc.

In the same way we can equate the interior and exterior expressions for E_θ and K_θ. We then obtain two equalities of Fourier series in $\exp(im\theta)$, in which, again, terms with different m decouple. These equations, which are not written out here, in combination with Eq. (C5) and its K_z counterpart are sufficient to produce the $\mathbf{R}$ matrices.

We first concentrate on interior reflection matrix $\tilde{\mathbf{R}}^-$; we obtain its coefficients by setting the exterior incoming field to zero: $\tilde{\mathbf{A}}^+ = 0$. It is now straightforward to solve, for a given m, the linear set of equation given to express A_m^{E-} and A_m^{K-} in terms of B_m^{E-} and B_m^{K-} by eliminating B_m^{E+} and B_m^{K+}. We obtain

$$A_m^{E-} = R_m^{EE-} B_m^{E-} + R_m^{EK-} B_m^{K-},$$

$$A_m^{K-} = R_m^{KE-} B_m^{E-} + R_m{}^{KK-} B_m^{K-}, \quad \text{(C6)}$$

with

$$R_m^{EE-} = \frac{1}{\delta_m}[(\alpha_{J^-H^+}^+ - \alpha_{H^+J^-}^-)(n_-^2 \alpha_{H^-H^+}^+ - n_+^2 \alpha_{H^+H^-}^-) - m^2 J_m^- H_m^- H_m^{+2} \tau^2],$$

$$R_m^{EK-} = \frac{1}{\delta_m}\left[\frac{2m\tau}{\pi k a}\frac{k_\perp^+}{k_\perp^-} H_m^{+2}\right],$$

$$R_m^{KE-} = -n_-^2 R_m^{EK-},$$

$$R_m^{KK-} = \frac{1}{\delta_m}[(\alpha_{H^-H^+}^+ - \alpha_{H^+H^-}^-)(n_-^2 \alpha_{J^-H^+}^+ - n_+^2 \alpha_{H^+J^-}^-) + m^2 J_m^- H_m^- H_m^{+2} \tau^2], \quad \text{(C7)}$$

where

$$\alpha_{J^\pm H^\pm}^{\pm} = \frac{k_\perp^{\pm}}{k} J_m'^{\pm} H_m^{\pm}, \quad \text{(C8)}$$

with other α coefficients defined analogously. Further,

$$\delta_m = (\alpha_{H^+J^-}^- - \alpha_{J^-H^+}^+)(n_-^2 \alpha_{J^-H^+}^+ - n_+^2 \alpha_{H^+J^-}^-) + (m J_m^- H_{m^+} \tau^2 \quad \text{(C9)}$$

$$\tau = \frac{\beta}{a k_\perp^- k_\perp^+}(n_+^2 - n_-^2). \quad \text{(C10)}$$

To obtain exterior reflection matrix $\tilde{\mathbf{R}}^+$ we set $\tilde{\mathbf{B}}^- = \mathbf{0}$ and eliminate the A_m^- coefficients. This yields

$$R_m^{EE-} = \frac{1}{\delta_m}[(\alpha_{J^-H^+}^+ - \alpha_{H^+J^-}^-)(n_-^2 \alpha_{J^-J^+}^+ - n_+^2 \alpha_{J^+J^-}^-) - m^2 J_m^+ H_m^+ H_m^{-2} \tau^2],$$

$$R_m^{EK+} = \frac{1}{\delta_m}\left[\frac{2m\tau}{\pi ka}\frac{k_\perp^-}{k_\perp^+}J_m^{-2}\right],$$

$$R_m^{KE+} = -n_+^2 R_m^{EK+},$$

$$R_m^{KK-} = -\frac{1}{\delta_m}[(\alpha_{J^-J^+}^+ - \alpha_{J^+J^-}^-)(n_-^2\alpha_{J^-H^+}^+ - n_+^2\alpha_{H^+J^-}^-) - m^2 J_m^+ H_m^+ H_m^{-2}\tau^2]. \quad \text{(C11)}$$

ACKNOWLEDGMENTS

This research was supported by the Australian Research Council. It has also benefited from travel support from the French and Australian governments.

REFERENCES

1. H. Kubota, K. Suzuki, S. Kawanishi, M. Nakazawa, M. Tanaka, and M. Fujita, "Low-loss, 2 km-long photonic crystal fiber with zero GVD in the near IR suitable for picosecond pulse propagation at the 800 nm band," in *Conference on Lasers and Electro-Optics (CLEO 2001)*, Vol. 56 of OSA Trends in Optics and Photonics (Optical Society of America, Washington, D.C., 2001), paper CPD3.
2. D. Mogilevtsev, T. A. Birks, and P. St. J. Russell, "Group-velocity dispersion in photonic crystal fibers," Opt. Lett. **23**, 1662–1664 (1998).
3. T. M. Monro, D. J. Richardson, N. G. R. Broderick, and P. J. Bennett, "Holey optical fibers: an efficient modal model," J. Lightwave Technol. **17**, 1093–1102 (2000).
4. J. C. Knight, J. Broeng, T. A. Birks, and P. St. Russell, "Photonic band gap guidance in optical fibers," Science **282**, 1476–1478 (1998).
5. T. A. Birks, J. C. Knight, and P. St. J. Russell, "Endlessly single-mode photonic crystal fiber," Opt. Lett. **22**, 961–963 (1997).
6. A. W. Snyder and J. D. Love, *Optical Waveguide Theory* (Chapman & Hall, London, 1996).
7. D. Marcuse, *Theory of Dielectric Optical Waveguides*, 2nd ed. (Academic, San Diego, Calif., 1991), Chap. 2.
8. M. Midrio, M. P. Singh, and C. G. Someda, "The space filling mode of holey fibres: an analytic vectorial solution," J. Lightwave Technol. **18**, 1031–1048 (2000).
9. F. Brechet, J. Marcou, D. Pagnoux, and P. Roy, "Complete analysis of the characteristics of propagation into photonic crystal fibers, by the finite element method," Opt. Fiber Technol. Mater., Devices Syst. **6**, 181–191 (2000).
10. A. Ferrando, E. Silvestre, J. J. Miret, and P. Andrés, "Vector description of higher-order modes in photonic crystal fibers," J. Opt. Soc. Am. A **17**, 1333–1340 (2000).
11. A. A. Maradudin and A. R. McGurn, "Out of plane propagation of electromagnetic waves in two-dimensional periodic dielectric medium," J. Mod. Opt. **41**, 275–284 (1994).
12. J. Broeng, T. Sondergaard, S. E. Barkou, P. M. Barbeito, and A. Bjarklev, "Waveguide guidance by the photonic bandgap effect in optical fibre," J. Opt. Pure Appl Opt. **1**, 477–482 (1999).
13. D. Mogilevtsev, T. A. Birks, and P. St. J. Russell, "Localized function method for modeling defect modes in 2-D photonic crystals," J. Lightwave Technol. **17**, 2078–2081 (2000).
14. B. J. Eggleton, P. S. Westbrook, C. A. White, C. Kerbage, R. S. Windeler, and G. L. Burdge, "Cladding-mode-resonances in air–silica microstructure optical fibers," J. Lightwave Technol. **18**, 1084–1100 (2000).
15. J. K. Ranka, R. S. Windeler, and A. J. Stentz, "Optical properties of high-delta air–silica microstructure optical fibers," Opt. Lett. **25**, 796–797 (2000).
16. K. M. Lo, R. C. McPhedran, I. M. Bassett, and G. W. Milton, "An electromagnetic theory of dielectric waveguides with multiple embedded cylinders," J. Lightwave Technol. **12**, 396–410 (1994).
17. E. Centeno and D. Felbacq, "Rigorous vector diffraction of electromagnetic waves by bidimensional photonic crystals," J. Opt. Soc. Am. A **17**, 320–327 (2000).
18. P. R. McIsaac, "Symmetry-induced modal characteristics of uniform waveguides. I. Summary of results," IEEE Trans. Microwave Theory Tech. **MTT-23**, 421–429 (1975).
19. M. J. Steel, T. P. White, C. M. De Sterke, R. C. McPhedran, and L. C. Botten, "Symmetry and degeneracy in microstructured optical fibers," Opt. Lett. **26**, 488–490 (2001).
20. D. Felbacq, G. Tayeb, and D. Maystre, "Scattering by a random set of parallel cylinders," J. Opt. Soc. Am. A **11**, 2526–2538 (1994).
21. E. Yamashita, S. Ozeki, and K. Atsuki, "Modal analysis method for optical fibers with symmetrically distributed multiple cores," J. Lightwave Technol. **3**, 341–346 (1985).
22. B. T. Kuhlmey, T. P. White, G. Renversez, D. Maystre, L. C. Botten, C. M. de Sterke, and R. C. McPhedran, "Multipole method for microstructured optical fibers. II. Implementation and results," J. Opt. Soc. Am. B **19**, 2331–2340 (2002).
23. W. Wijngaard, "Guided normal modes of two parallel circular dielectric rods," J. Opt. Soc. Am. **63**, 944–949 (1973).
24. C.-S. Chang and H.-C. Chang, "Theory of the circular harmonics expansion method for multiple-optical-fiber system," J. Lightwave Technol. **12**, 415–417 (1994).
25. M. Abramowitz and I. A. Stegun, *Handbook of Mathematical Functions* (Dover, New York, 1965).
26. D. Maystre and P. Vincent, "Diffraction d'une onde electromagnetique plane par an object cylindrique non infinitement conducteur," Opt. Commun. **5**, 327–330 (1972).
27. W. H. Press, B. P. Flannery, S. A. Teukolsky, and W. T. Vetterling, *Numerical Recipes* (Cambridge U. Press, Cambridge, 1986), Sec. 2.9.
28. L. Schwartz, *Mathematics for the Physical Sciences* (Addison-Wesley, Reading, Mass., 1966).